Journal of Alloys and Compounds 506 (2010) 581–588

Contents lists available at ScienceDirect

Journal of Alloys and Compounds

journal homepage: www.elsevier.com/locate/jallcom

Structural and mechanical characterization of rapidly solidified $Al_{95}Ni_5$ and $Al_{93}Ni_5Mm_2$ alloys prepared by centrifugal atomization

D. Vojtěch*, F. Průša, A. Michalcová

Department of Metals and Corrosion Engineering, Institute of Chemical Technology, Prague, Technická 5, 166 28 Prague 6, Czech Republic

ARTICLE INFO

Article history:
Received 9 June 2010
Received in revised form 7 July 2010
Accepted 9 July 2010
Available online 15 July 2010

Keywords:
Metals and alloys
Nanostructured materials
Rapid solidification
Microstructure
Mechanical properties

ABSTRACT

$Al_{95}Ni_5$ and $Al_{93}Ni_5Mm_2$ (at.%) alloys were prepared by induction melting and centrifugal atomization. Both as-cast and rapidly solidified (RS) alloys were studied by various techniques, including light, scanning and transmission electron microscopy, energy dispersion spectrometry, differential scanning calorimetry and X-ray diffraction analysis. Room temperature hardness was measured for the rapidly solidified alloys, as well as after their long-term annealing at 400 °C. It is observed that the RS alloys are crystalline. The binary Al–Ni alloy consists of Al and Al_3Ni phases, while in the ternary Al–Ni–Mm alloy, there are Al dendrites supersaturated with Ni, Al_3Ni and non-equilibrium $\alpha Al_{11}(Mm,Ni)_3$ phases. Average Al dendrite arm thickness is about 100 nm. Both supersaturated Al and $\alpha Al_{11}(Mm,Ni)_3$ decompose upon heating at 300–450 °C. Room temperature hardness of the RS $Al_{95}Ni_5$ and $Al_{93}Ni_5Mm_2$ alloys are 150 and 300 HV, respectively. These values are discussed in relation to various hardening mechanisms. Thermal stability of both alloys is low, due a rapid structural coarsening and hardness reduction during annealing at 400 °C.

1. Introduction

Aluminum alloys are prospective materials for light-weight structural applications. Generally, tensile strength of commercial Al-based wrought alloys does not exceed about 700 MPa. This strength level can be achieved by an appropriate thermomechanical treatment combining cold working and precipitation hardening. It seems that 700 MPa is a limit of Al-based alloys in which classical hardening mechanisms, such as solid solution hardening, grain boundary hardening, precipitation hardening, operate. Another limitation of Al-based alloys is their poor thermal stability, meaning that mechanical characteristics rapidly reduce, as temperature increases above approx. 200 °C. One exception is a group of alloys containing small additions of scandium that show excellent stability at elevated temperatures. However, these alloys are still far from the mass commercial level, because of a very high price of scandium metal.

It was reported many times during the last two decades, that rapidly solidified (RS) Al–TM–RE alloys (TM = transition metals like Ni, Mn, Ti, Cr, Fe, V and other; RE = rare earth metals like La, Ce, Nd, etc.) can achieve strength levels much exceeding the limit of commercial Al alloys [1–6]. High strength of these materials is generally attributed to amorphous or nano-crystalline structure that is extremely resistant to dislocation movement. There are a lot of studies devoted to RS Al–TM–RE alloys. However, among these alloys, only several systems can form amorphous phase during melt spinning or melt atomization. The glass forming ability (GFA) is generally enhanced with increasing number of alloying elements, large atomic size mismatch and negative heats of mixing of Al and additives [7]. When an alloy shows a low GFA, RS structure generally consists of nano-crystalline or nano-quasi-crystalline phases [8]. From the thermal stability point of view, positive role of TM is associated with their low solid solubility and slow diffusivity in Al. Al–Cr-based alloys appear as very prospective to replace heavier steels or Ti alloys in some thermally loaded applications [9].

In this study we focused our attention on RS Al–Ni–Mm alloys (Mm = mishmetal consisting of RE, such as Ce, La, Nd and Pr). RS Al–Ni–RE alloys have been extensively studied so far and it has been demonstrated that they fall into a group of alloys showing high GFA and, therefore, excellent mechanical properties [10–12]. In contrast to most of studies reported so far, we investigate an alloy containing a relatively low atomic percentage of Mm in this study, because high costs of RE metals are main barriers for mass production and application of Al–TM–RE alloys. Among rapid solidification techniques available at present, we selected centrifugal atomization in our experiment. In this technique a melt is atomized into powder by a fast rotating disc. In contrast to commonly used pressure gas atomization technique which produces almost spherical powder particles, centrifugal atomization produces flake-like

* Corresponding author. Tel.: +420 220444290; fax: +420 220444400.
E-mail address: Dalibor.Vojtech@vscht.cz (D. Vojtěch).

0925-8388/$ – see front matter © 2010 Elsevier B.V. All rights reserved.
doi:10.1016/j.jallcom.2010.07.081

Table 1
Chemical composition of investigated alloys (in at.%).

Alloy	Ni	Mm	Al
$Al_{95}Ni_5$	5.2	–	Bal.
$Al_{93}Ni_5Mm_2$	5.4	2.2	Bal.

particles showing a very low thickness. It is assumed that such particle shape will facilitate powder compaction.

2. Experimental

In this study we investigated two alloys with nominal compositions $Al_{95}Ni_5$ and $Al_{93}Ni_5Mm_2$ (hereafter, all concentrations are in at.%, unless otherwise stated). Symbol Mm denotes mishmetal, i.e. an alloy consisting of 45% Ce, 38% La, 12% Nd and 5% Pr. Both alloys were prepared by melting a pure Al (99.9% purity), nickel (99.8% purity) and Mm (99.5% purity) in an induction furnace under argon protective atmosphere. Obtained ingots were analyzed by X-ray fluorescence spectrometry (XRF) and results are summarized in Table 1.

Rapidly solidified powders of both alloys were prepared by centrifugal atomization. In this technique, a melt flows through a thin graphite nozzle onto the centre of a fast rotating (15 000 rpm) graphite disc. When the melt comes into contact with disc, it is atomized by a strong centrifugal force into droplets which are ejected towards a water cooled wall of atomizer where they rapidly solidify. As stated before, this type of atomization produces flake-like powder particles with thickness ranging from 10 to 50 μm and maximum size up to several mm. Morphology of prepared powders is presented in Fig. 1.

Prepared powders were sieved to obtain various granulometric fractions from <0.25 to >2.8 mm. For further study we selected granulometric fractions below 1.4 mm. Structural examinations of ingots and RS powders were carried out by using a light microscope (LM), scanning electron microscope (SEM, Hitachi S 4700, accelerating voltage 15 kV) equipped with energy dispersion spectrometer (EDS, Noran) and a transmission electron microscope (TEM, Jeol 3010, accelerating voltage 300 kV) equipped with EDS (Oxford Instruments). TEM foils were prepared from coarse particles by electropolishing in a mixture of ethanol and nitric acid (3:1 by volume) at 20 °C. Phase composition was determined by X-ray diffraction (XRD, Xîpert Pro). Differential scanning calorimetry (DSC, Setaram, temperature range 25–500 °C, heating rate 10 °C/min) was used to monitor solid state transformations occurring in the powders on heating. Structural investigations of powders were completed by Vickers microhardness measurements (HV 0.005) of both rapidly solidified and annealed powders. Long-time annealing at 400 °C/300 h was used to estimate thermal stability of alloys.

3. Results and discussion

3.1. Structure of the as-cast ingots

Fig. 2 presents SEM micrograph of the cast $Al_{95}Ni_5$ alloy ingot together with an X-ray map of Ni distribution. One can see that the structure consists of coarse elongated primary Al_3Ni phase and $Al_3Ni + Al$ eutectic, see also XRD patterns in Fig. 4. According to the Al–Ni phase diagram [13], this type of structure corresponds to the hypereutectic composition of the alloy. SEM microstructure and elemental distribution of the as-cast ternary $Al_{93}Ni_5Mm_2$ ingot is shown in Fig. 3. Apparently, there are two types of primary phases, one enriched in Ni (gray) and another enriched in Mm (white). Point chemical analyses of these two phases are summarized in Table 2. According to this Table, to the Al–Ni, Al–Ce, Al–La and Al–Nd binary phase diagrams [13] and to the XRD analysis shown in Fig. 4, these phases are Al_3Ni and $\alpha Al_{11}Mm_3$. The latter phase can be regarded as a solid solution of isostructural orthorhombic $\alpha Al_{11}Ce_3$ and $\alpha Al_{11}La_3$. In Table 3, crystallographic parameters of present phases are summarized and it is seen that lattice parameters of $\alpha Al_{11}Ce_3$ and $\alpha Al_{11}La_3$ phases are very similar which supports their solid solubility [14]. One can also see in Table 2 that solubilities of Ni in $\alpha Al_{11}Mm_3$ and of Mm in Al_3Ni are negligible. In addition to the coarse primary phases, in the struc-

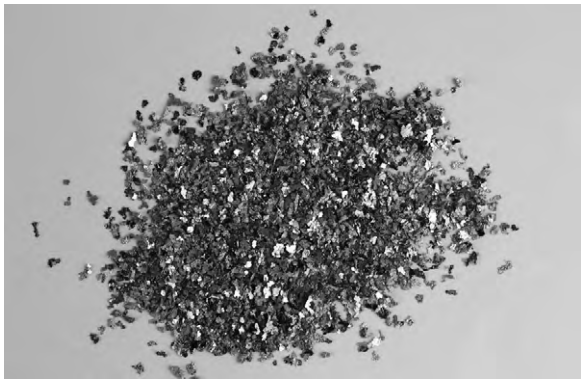

Fig. 1. Morphology of powder prepared by centrifugal atomization.

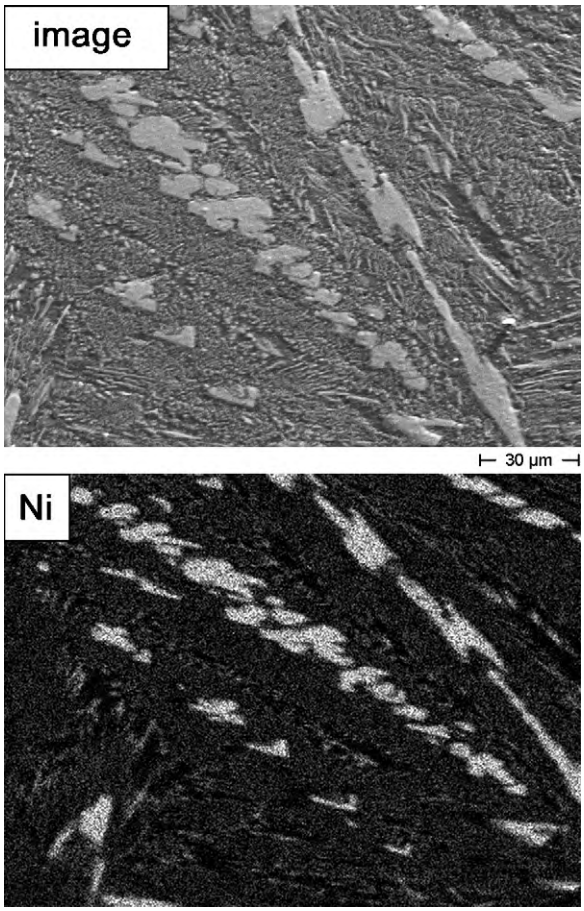

Fig. 2. SEM micrograph and Ni distribution map of the as-cast $Al_{95}Ni_5$ alloy.

Table 2
Local chemical compositions (in at.%) at points marked in Fig. 3.

Point no.	Element		
	Al	Ni	Mm
1	74.01	25.85	0.14
2	75.22	0.04	24.74

Table 3
Crystallographic parameters of phases present in the Al–Ni–Mm alloy [14].

Phase	Crystal structure	Space group	Lattice parameters (Å)		
			a	*b*	*c*
Al	fcc	*Fm3m*	4.049	–	–
Al_3Ni	Orthorhombic	*Pnma*	6.598	7.352	4.802
$Al_{11}Ce_3$	Orthorhombic	*Immm*	4.395	13.025	10.092
$Al_{11}La_3$	Orthorhombic	*Immm*	4.431	13.142	10.132

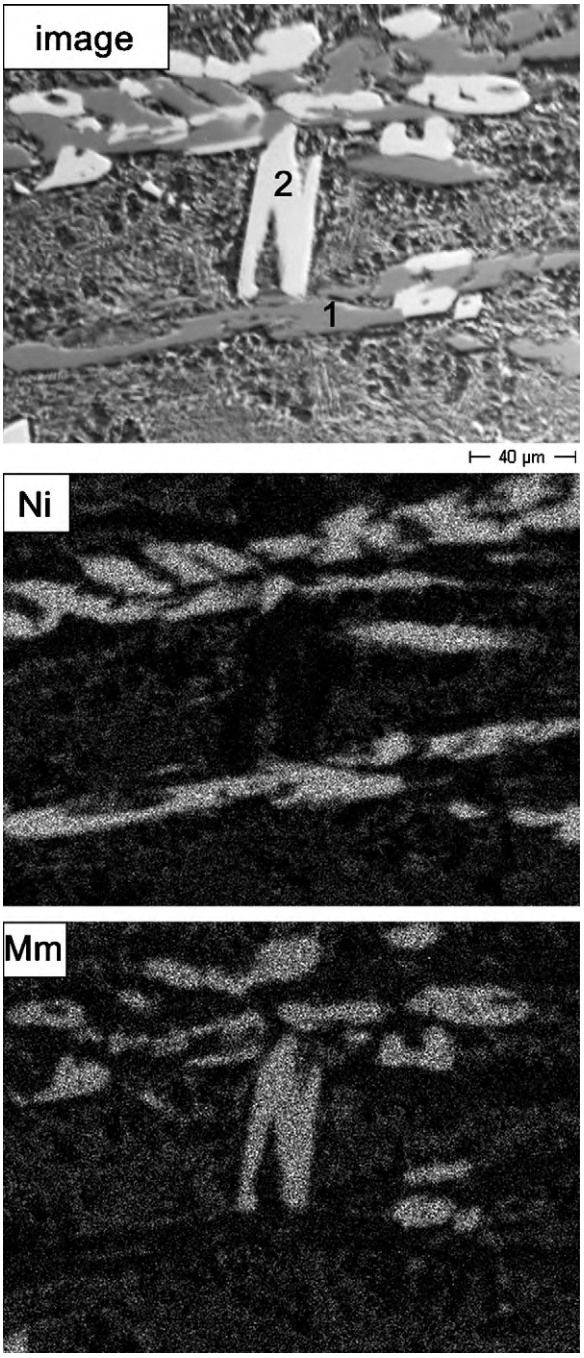

Fig. 3. SEM micrograph and elemental distribution maps of the as-cast $Al_{93}Ni_5Mm_2$ alloy.

ture of the $Al_{93}Ni_5Mm_2$ alloy there is a ternary eutectic consisting of $Al + Al_3Ni + \alpha Al_{11}Mm_3$ phases. Since Mm is dominated by cerium, the ternary Al–Ni–Mm system can be roughly approximated by the Al–Ni–Ce system. Invariant ternary eutectic crystallization in this system producing $Al + Al_3Ni + \alpha Al_{11}Ce_3$ eutectic occurs at 628 °C and a ternary eutectic composition is 1.6% Ce and 2.1% Ni [7]. Neither EDS (Table 2) nor XRD analysis (Fig. 4) prove the presence of any ternary phase in the as-cast Al–Ni–Mm alloy. This agrees well with ternary Al–Ni–Ce phase diagrams constructed recently by several authors [7,15,16]. As an example, an Al–Ni–Ce phase diagram at 500 °C calculated by Tang et al. [7] is presented in Fig. 5. In this diagram, there is a broad concentration range in which only binary Al–Ni and Al–Ce phases appear together with Al. One can estimate, that, in the as-cast state, the formation of a ternary phase in $Al_{95-X}Ni_5Ce_X$ alloys would require cerium concentrations X exceeding about 15%.

3.2. Structure of the RS alloys

Optical micrographs of two granulometric fractions separated from both alloys are presented in Fig. 6. One can see that both alloys have heterogeneous crystalline structure, i.e. they are not fully amorphous, despite a large GFA of the Al–Ni–Mm system [10,11]. Fig. 6a and b compare two granulometric fractions (0.7–1.4 and <0.25 mm) of the binary $Al_{95}Ni_5$ alloy. It is observed that the structures are composed of almost equi-axed particles of intermetallic phases (gray) dispersed in Al matrix (light). Intermetallic particle size ranges from sub-micrometer level to about 10 μm. Important observation is that dimensions and morphology of intermetallic phases do not depend on the size of granulometric fraction significantly. This is an interesting difference between centrifugal atomization used in our experiment and the classical pressure gas atomization producing spherical particles. In the latter case, it is well known that there is a direct relationship between particle size and internal structure. The smaller the powder particles, the finer the structure and the more metastable the present phases [17]. The reason is in a rapid cooling of small particles by a stream of atomizing gas that results in a deep undercooling of a melt under solidus and, therefore, in a fast solidification. Larger droplets are cooled down more slowly and a resulting structure is coarser. On the other hand, mechanism of the centrifugal atomization is quite different. Melt falls onto a fast rotating disc where it is atomized by centrifugal force into droplets of various dimensions. These droplets are ejected towards the wall of atomization chamber where they rapidly solidify to form the characteristic flake-like shape. It was indicated in Experimental part that the thickness and, therefore, cooling rate of flakes do not depend on their diameter significantly. Therefore, structural variations caused by particle size differences are minimal.

Fig. 6c and d shows microstructure of RS $Al_{93}Ni_5Mm_2$ alloy. As in the previous case, two powder fractions 0.7–1.4 and <0.25 mm are compared to reveal a possible influence of particle size on the structure. One can see that structures contain large fractions of intermetallic phases in aluminum matrix. Dimensions of intermetallic phases lie between sub-micrometer level and about 20 μm. Their shapes range from elongated to almost spherical. Similarly to the binary alloy presented in Fig. 6a and b, average size of intermetallic phases does not change significantly with powder particle size.

More detailed views of the RS alloys are provided by electron microscopy. In Fig. 7, there are SEM micrographs and elemental maps of the RS alloys. As also indicated in Fig. 6, the binary $Al_{95}Ni_5$ alloy contains Ni-rich particles dispersed in Al matrix, see Fig. 7a. In contrast, the ternary alloy contains at least two types of intermetallic phases, one being enriched in Ni and another enriched in Mm, as shown in Fig. 7b. XRD patterns of two granulometric fractions of the RS alloys are summarized in Fig. 4. It is seen that all XRD patterns contain sharp and well-separated peaks, confirming the crystalline nature of RS alloys. The peaks can be assigned to Al, Al_3Ni and $\alpha Al_{11}Mm_3$ phases, similarly to the as-cast state (Table 3). Therefore, the phase composition agrees with the ternary phase diagram presented in Fig. 5, despite the rapid cooling and fine structure. Amorphous phase which would lead to the appearance of a broad halo in XRD patterns is not detected. Moreover, as indicated before, there is no dependence of phase composition on powder particle size.

DSC records of RS alloys are plotted in Fig. 8. These records confirm the findings above, because they are free of exothermal effects at low temperatures of about 150–300 °C which would correspond

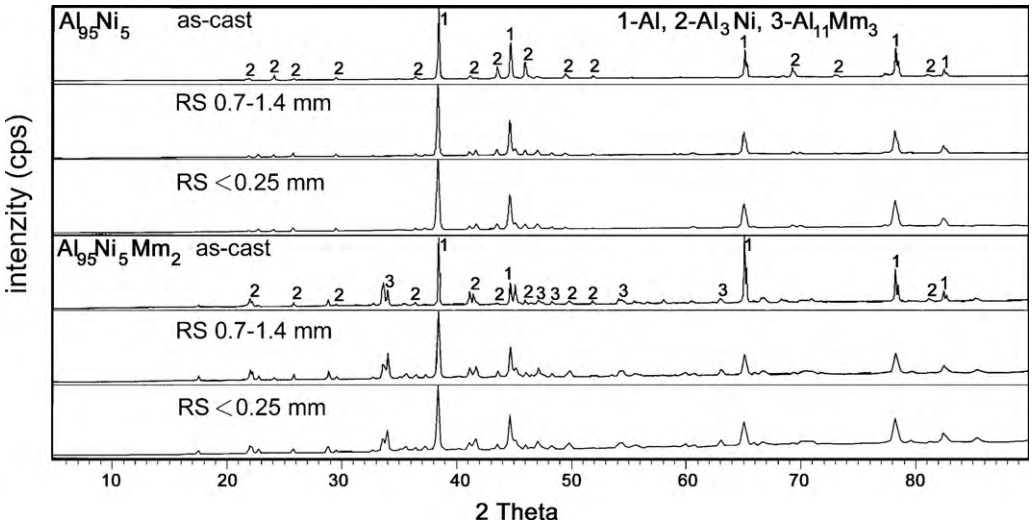

Fig. 4. XRD patterns of the as-cast and rapidly solidified (RS) alloys.

to the primary crystallization of an Al–Ni–Ce(La) amorphous phase [1,4,18]. Instead, in the case of ternary $Al_{93}Ni_5Mm_2$ alloy there is a very slight and broad exothermal effect at about 300–450 °C. This temperature is too high to be associated with primary crystallization of Al. More likely, the exothermal effect can be attributed to the decomposition of a non-equilibrium phase and supersaturated Al-solid solution, as will be given later.

The absence of amorphous phase in the RS $Al_{93}Ni_5Mm_2$ alloy can be explained in terms of chemical composition. It is generally agreed that the formation of glassy phase would require higher nickel and, particularly mishmetal, concentrations. Recently reported compositional dependence of amorphous phase occurrence in the Al–Ni–Ce system is shown in Fig. 9 [7]. This diagram implies that the investigated $Al_{93}Ni_5Mm_2$ alloy does probably not fall into this glassy region, because of a similarity between Mm and Ce. If one wants to obtain a glassy structure, a minimum Ce- and Ni-concentrations of about 5% would be needed [7]. If Ce-concentration is only 2%, the suppression of crystallization would require about 8% Ni [2]. Sufficient Ni- and Mm-concentrations would prevent the formation of a long-range ordered atomic arrangements and crystallization during cooling. This is generally explained on the base of a large atomic size mismatch between Ce (atomic size of 1.181 nm [1]) and other elements (atomic size of Al and Ni are 0.143 and 0.124 nm, respectively [1]) and negative heats of mixing of elements. The former factor leads to stabilization of a low energy and high viscosity liquid due to the formation of closely packed local structures. Negative heats of mixing stabilize the formation of short-range order Al–Ni and Al–Mm clusters in a melt, thus suppressing long-range diffusion of atoms and crystallization. Apparently, in our case atomic concentrations of rare earth metals are too low to efficiently stabilize chemical short-range ordering of liquid.

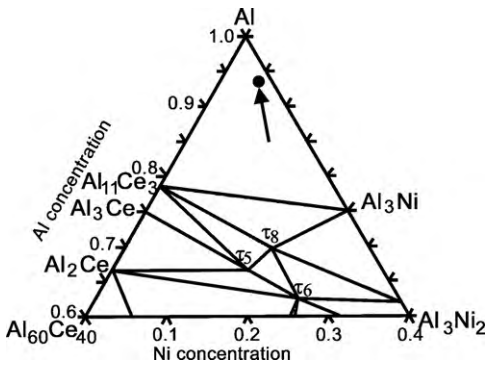

Fig. 5. Ternary phase diagram of Al–Ni–Ce system at 500 °C [7] (chemical composition of the investigated ternary alloy is marked by an arrow, τ denotes ternary phases).

In order to characterize the structure of ternary $Al_{93}Ni_5Mm_2$ alloy, particularly of aluminum matrix, more precisely, TEM was employed. The advantage of EDS analysis in combination with TEM is that analyzed volumes are much smaller as compared to the similar analysis in SEM. Therefore, local chemical compositions in sub-micrometer sized regions can be determined much more accurately by this method. TEM images of the RS $Al_{93}Ni_5Mm_2$ alloy and chemical compositions in marked points are presented in Fig. 10 and Table 4, respectively. In Fig. 10a and b, there are coarse primary intermetallic phases surrounded by Al-rich matrix. Point analysis (Table 4) shows that the first primary intermetallic phase (point 1) corresponds to the Al_3Ni in which a solubility of Mm is negligible. In contrast, chemical composition of the second one (Fig. 10b, point 2) suggests that it is the $\alpha Al_{11}Mm_3$ phase but strongly enriched in Ni, so that its formula may be written as $\alpha Al_{11}(Mm,Ni)_3$. The partial replacement of rare earth atoms by Ni can be attributed to the rapid solidification, because such replacement is not observed for the as-cast state, see Table 2. During rapid solidification, Al–Ni and Al–Mm clusters present in the melt may serve as sites at which Al_3Ni and $\alpha Al_{11}(Mm)_3$ phases nucleate. Several authors have indicated that Al–Ni interactions are stronger than Al–Ce(Mm) [1]. Therefore, once a critical nucleus of the $\alpha Al_{11}(Mm)_3$ phase forms and grows rapidly, Al–Ni bonds originally present in the melt may be partially retained in this nucleus due to a short diffusion time. On the other hand, in growing Al_3Ni nuclei, stronger Al–Ni bonds efficiently replace Al–Mm bonds originally present in clusters and, therefore, concentration of Mm in Al_3Ni phase is negligible. The $\alpha Al_{11}(Mm,Ni)_3$ phase can be regarded as non-equilibrium and metastable, because of a low equilibrium solubility of Ni in $\alpha Al_{11}(Mm)_3$ [15]. As a result, this

Table 4
Chemical compositions at points depicted in Fig. 10 (EDS).

Point no.	Element (in at.%)		
	Al	Ni	Mm
1	76.84	23.16	–
2	81.89	4.61	13.50
3	99.08	0.92	–
4	79.26	11.55	9.19

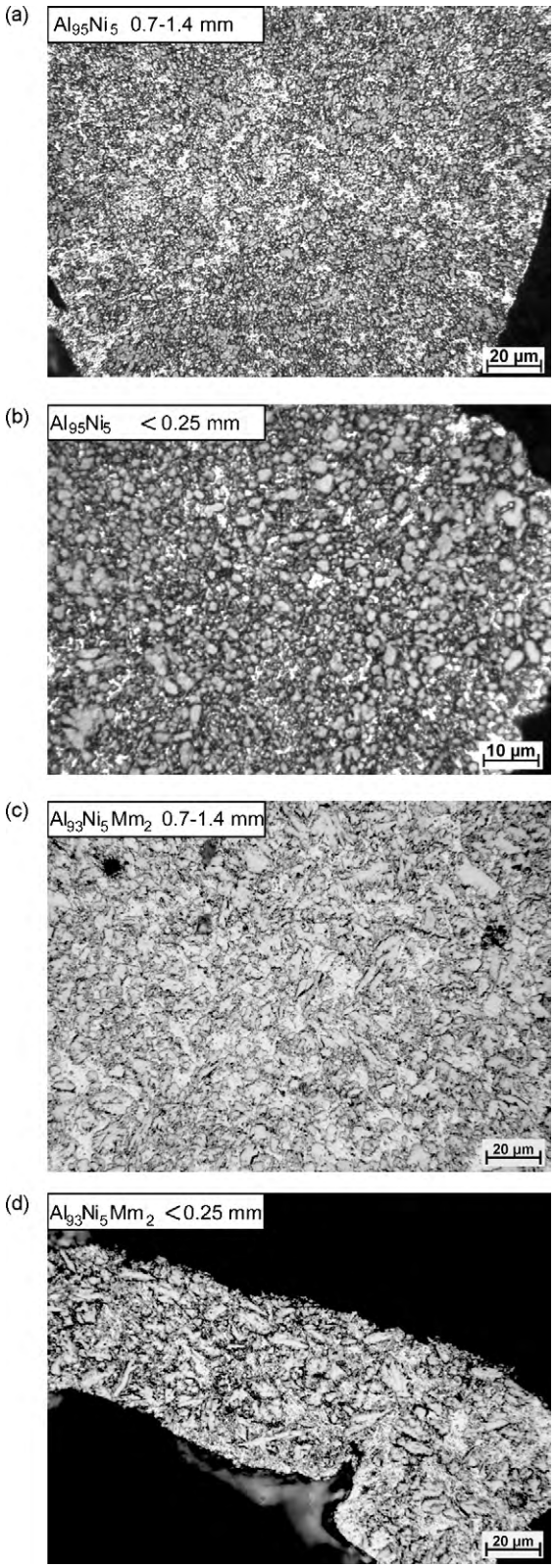

Fig. 6. Optical micrographs of RS $Al_{95}Ni_5$ (a and b) and $Al_{93}Ni_5Mm_2$ (c and d) alloys.

phase may decompose upon heating to form $\alpha Al_{11}(Mm)_3$ + Ni that may be accompanied by a thermal effect. As shown in Fig. 8, there is a thermal effect occurring at about 300–450 °C. It is believed that this effect is probably a superposition of two events: (1) decomposition of intermetallic phase stated above and (2) decomposition of a supersaturated solid solution, see below.

Fig. 10c showing a TEM micrograph of Al matrix reveals a dendritic morphology of fcc Al phase with primary and secondary dendrite arms. More detailed view presented in Fig. 10d indicates that an average dendrite arm thickness is about 100 nm. Point chemical microanalysis was carried out both in the centre of a dendrite arm (point 3) and in an interdendritic region (point 4). Results given in Table 4 indicate that aluminum phase is supersaturated with nickel, because of a negligible solid solubility of Ni in Al in equilibrium state [13]. The Ni-supersaturation can be directly related to the rapid cooling and dendrite growth during which solute trapping occurs at a fast moving solid/liquid interface [19]. Nickel atoms readily substitute aluminum in fcc lattice due to a similarity between Ni and Al atomic radii (0.124 and 0.143 nm, respectively [1]). Upon heating, supersaturated solid solution becomes unstable and decomposes that is associated with a thermal effect, as shown in DSC curve in Fig. 8. In contrast to nickel, rare earth atoms are much larger than aluminum and their incorporation into fcc lattice of Al would lead to excessive internal stress. Therefore, concentra-

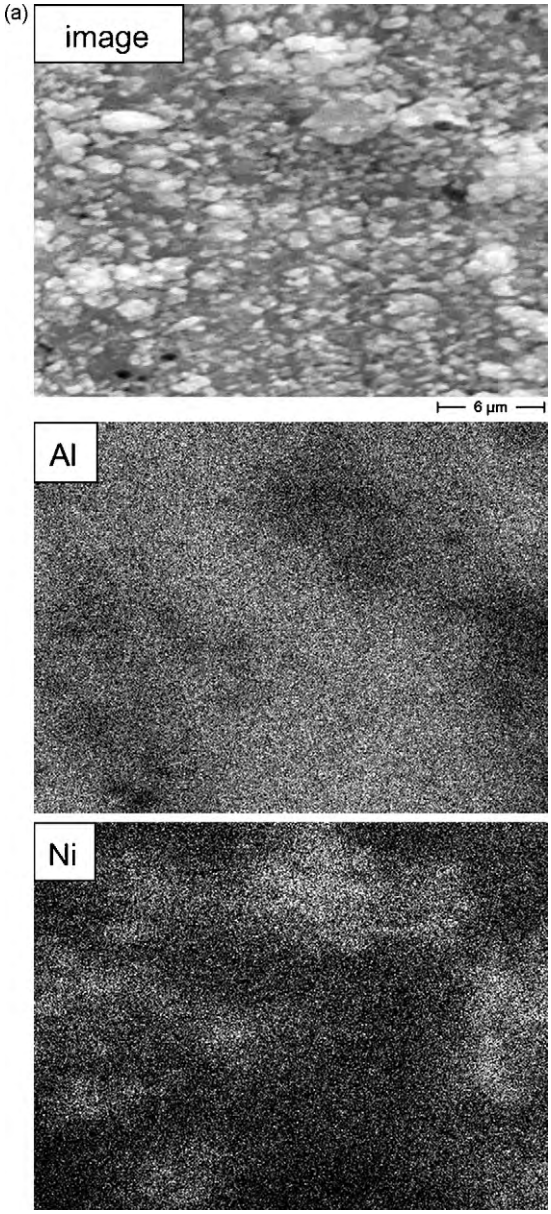

Fig. 7. SEM micrographs and elemental maps of RS $Al_{95}Ni_5$ (a) and $Al_{93}Ni_5Mm_2$ (b) alloys (granulometric fraction of 0.7–1.4 mm).

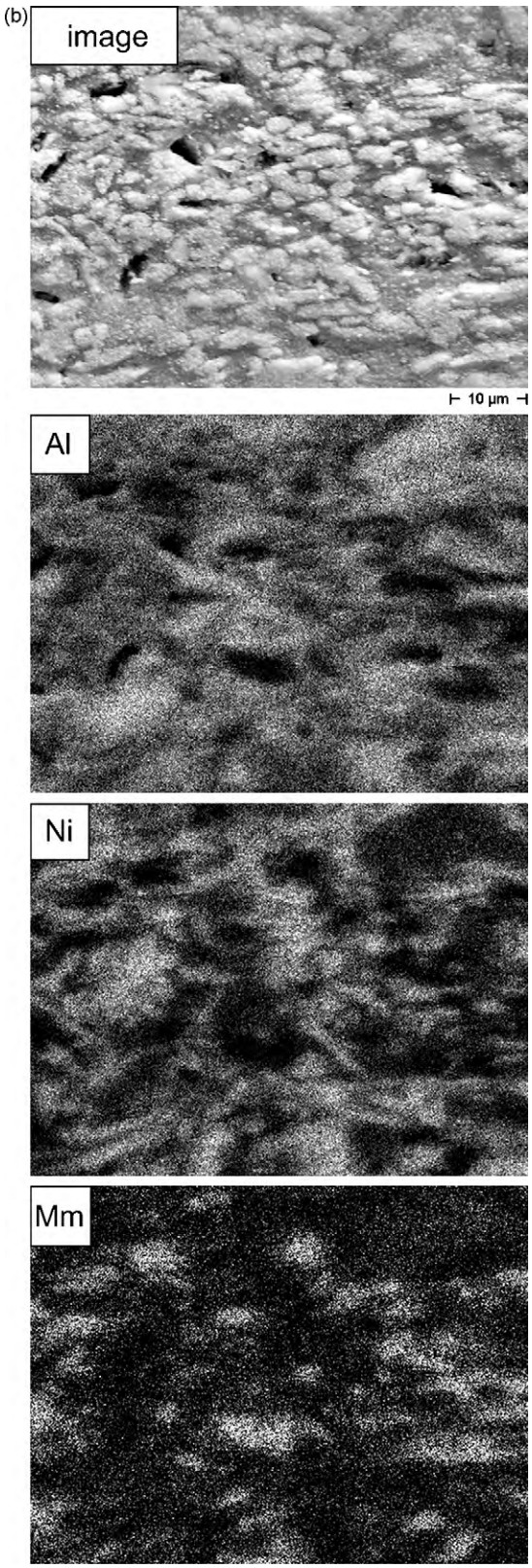

Fig. 7. (*Continued*).

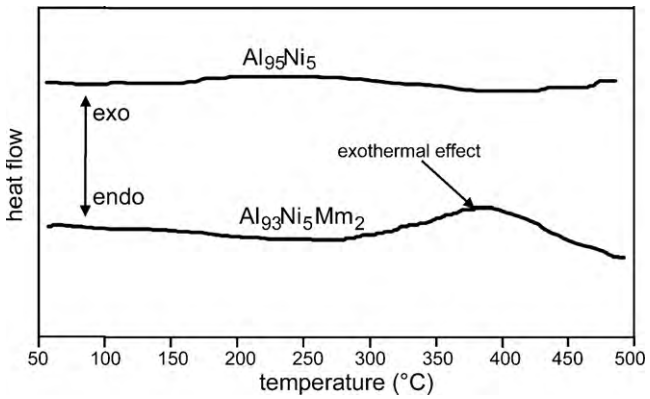

Fig. 8. DSC records of RS alloys (granulometric fraction of <0.25 mm).

tion of Mm in Al dendrites, even after rapid solidification, is low, see Table 4, point 3.

3.3. Hardness of the RS alloys

Fig. 11 presents the room temperature microhardness of both alloys after various times of annealing at 400 °C. One can see that, in the RS state, both alloys differ significantly. Hardness of the binary $Al_{95}Ni_5$ alloy is about 150 HV. In contrast, the ternary $Al_{93}Ni_5Mm_2$ alloy shows a hardness of more than 300 HV, i.e. double that of the binary counterpart. For aluminum alloys, there is an approximate relationship between Vickers hardness HV and yield strength YS:

$$YS \approx 3 \cdot HV \quad (1)$$

In our experiment we measured microhardness, so that Eq. (3) can only be used as a rough estimate. According to this estimate, the measured microhardness of the binary and ternary alloys would correspond to yield strength of about 450 and 900 MPa, respectively! Of course, such a high strength of a bulk ternary alloy could only be obtained by using a proper parameters of powder compaction, i.e. low temperatures and short times, to retain as much structural features of the RS state as possible.

Generally, Al-based alloys show four main hardening (strengthening) mechanisms: (1) Hall–Petch hardening due to grain boundaries, (2) Orowan hardening caused by hard particles, (3)

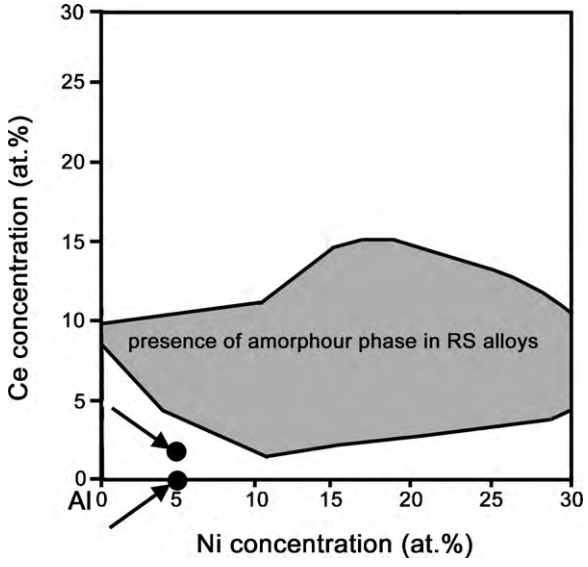

Fig. 9. Compositional map of the glassy state (gray area) in Al–Ni–Ce system [7] (compositions of the investigated alloys are indicated by arrows).

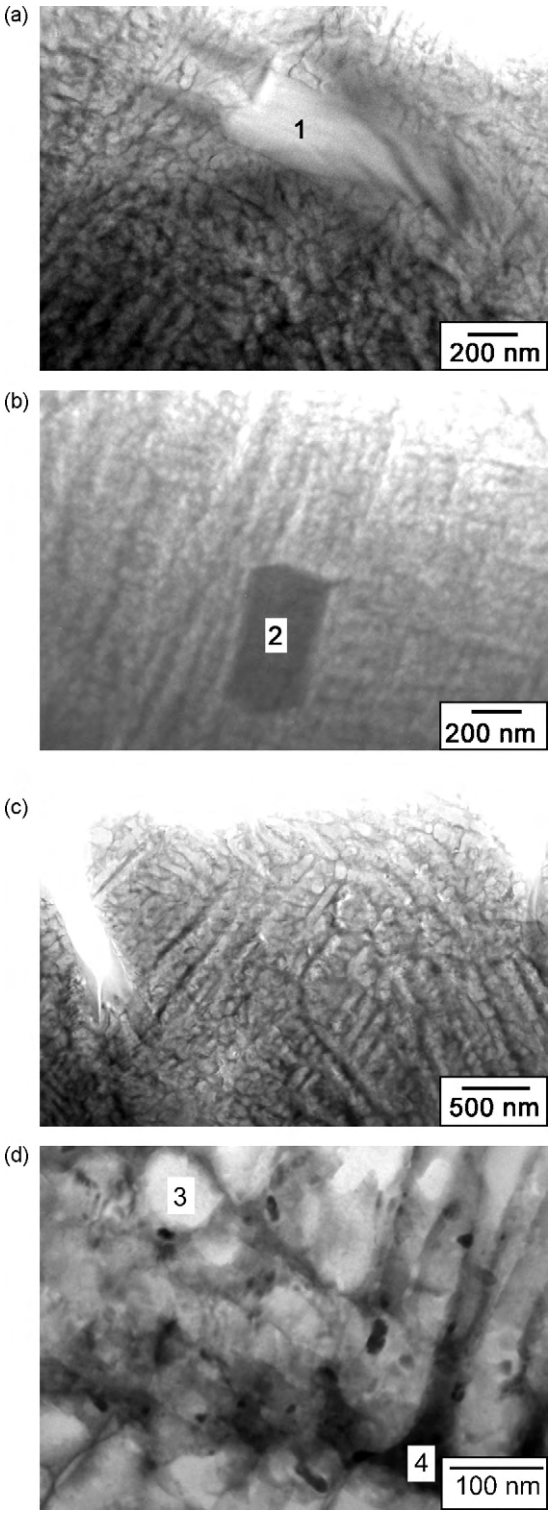

Fig. 10. TEM micrographs of the RS $Al_{93}Ni_5Mm_2$ alloy (granulometric fraction of 0.7–1.4 mm) with points at which local chemical compositions were measured.

solid solution hardening resulting from the presence of solute atoms in Al lattice and (4) precipitation hardening due to coherent or semicoherent precipitates. In the RS $Al_{93}Ni_5Mm_2$ alloy, the last contribution can be neglected, since no precipitates are observed in the structure, see Fig. 10. The Hall–Petch (H–P) contribution to yield strength $\Delta\sigma_{HP}$ can be written as:

$$\Delta\sigma_{HP} = k \cdot d^{-1/2}, \quad (2)$$

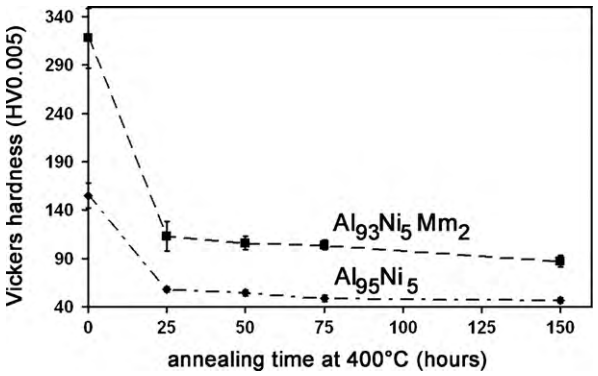

Fig. 11. Plots of room temperature Vickers hardness of the investigated RS alloys versus annealing time at 400 °C.

where k is the Hall–Petch coefficient and d is the grain size. It has been reported in [20] that the H–P coefficients k for Al–TM alloys range from 150 to 170 MPa $\mu m^{1/2}$. By using the average grain size of 0.1 μm, see Fig. 10, then Eq. (2) gives $\Delta\sigma_{HP}$ of 470–540 MPa that corresponds to a hardening by about 160–180 HV. The Orowan contribution due to hard intermetallic phases $\Delta\sigma_O$ can be roughly estimated as:

$$\Delta\sigma_O = \frac{3 \cdot Gb}{L}, \quad (3)$$

where G, b and L are the shear modulus of the matrix (26 GPa), the Burgers vector (0.286 nm) and the average interparticle spacing, respectively [21,22]. As shown in Figs. 6, 7 and 10, the ternary alloy contains particles ranging from tens nanometers (Fig. 10d) to several micrometers (Fig. 6). Large particles do not hinder dislocation slip efficiently. Therefore, in Eq. (3), we use an interparticle spacing of 200 nm that is a spacing between the smallest primary inter-

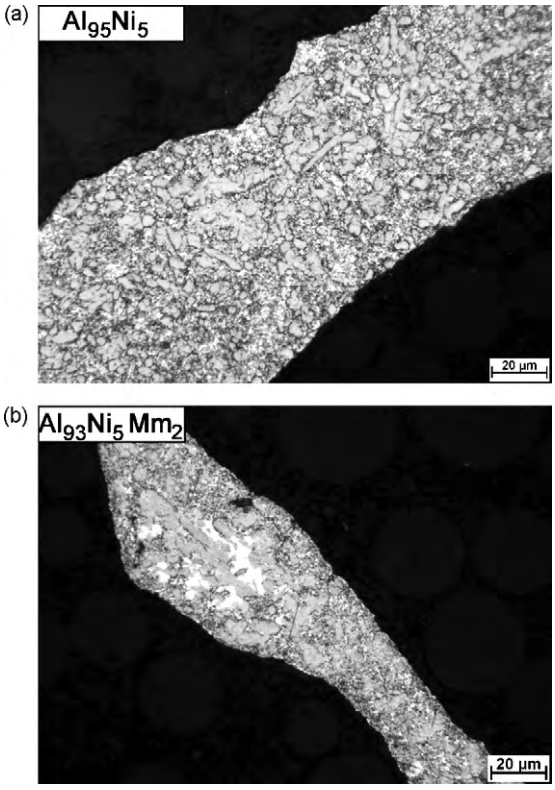

Fig. 12. Optical micrographs of $Al_{95}Ni_5$ (a) and $Al_{93}Ni_5Mm_2$ (b) alloys annealed at 400 °C for 300 h.

metallic phases observed as dark spots in Fig. 10d. Despite the short interparticle spacing used in our calculation, an estimated Orowan strengthening is relatively low, about 110 MPa, giving a hardening of ≈40 HV. The third strengthening mechanism is caused by solute atoms, in our case mainly Ni (Fig. 10, Table 4), dissolved in Al-based solid solution. It can be anticipated that this contribution is also small, because of a similarity in atomic size of Ni and Al and a relatively low Ni concentration in solid solution (Table 4). Based on the above statements, the high hardness of the ternary $Al_{93}Ni_5Mm_2$ alloy can be mainly attributed to the refined dendritic structure of Al matrix. Although hard intermetallic phases of micrometer size do not represent any significant barrier for dislocation movement, they certainly contribute to the total hardness due to their large volume fraction. For production of a high-strength bulk alloy, it is very important to retain the refined structure of Al after compaction.

It can bee seen in Fig. 11 that the alloys show a poor thermal stability, because the hardness rapidly reduces already during the first 25 h of annealing. The softening process is particularly fast for the ternary alloy. The observed hardness reduction is attributable to coarsening of phases present in the structure, as is evident from comparison of Figs. 6 and 12 that present RS and annealed structures, respectively. In the latter case, there are particles of intermetallic phases exceeding 40 μm in size, whereas particles in the RS ternary alloy scarcely achieve 20 μm.

4. Conclusions

It is shown in this work that the concentrations of alloying elements in the $Al_{93}Ni_5Mm_2$ alloy is not enough to stabilize glassy amorphous structure after rapid solidification. Instead, the structure being between nano- and micro-crystalline consists of very fine dendritic aluminum based matrix and dispersed intermetallic phases. Rapid solidification brings about supersaturation of Al-solid solution with Ni and a modification of chemical composition of Al–Mm crystalline phase. The refined structure and a high fraction of intermetallics result in a relatively high hardness of the RS ternary alloy. It is expected that a bulk alloy significantly exceeding the strength of commercial materials can be prepared, provided that a compaction process does not modify the RS structure significantly. Research on compaction of RS powders prepared by centrifugal atomization are now in progress.

Acknowledgements

Authors wish to thank the Ministry of Education, Youth and Sports of the Czech Republic (project no. MSM6046137302 and MSMT no. 21/2010) and the Czech Academy of Sciences (project no. KAN 300100801) for their financial supports of this research.

References

[1] C. Triveno Rios, S. Surinach, M.D. Baró, C. Bolfarini, W.J. Botta, C.S. Kiminami, J. Non-Cryst. Solids 354 (2008) 4874–4877.
[2] M.A. Munoz-Morris, S. Surinach, L.K. Varga, M.D. Baro, D.G. Morris, Scripta Mater. 47 (2002) 31–37.
[3] A. Inoue, Mater. Sci. 43 (1998) 365–520.
[4] K.L. Sahoo, M. Wollgarten, J. Haug, J. Banhart, Acta Mater. 53 (2005) 3861–3870.
[5] R. Sahu, A.J. Kailath, S. Chatterjee, K.L. Sahoo, Mater. Sci. Eng. A527 (2010) 1339–1342.
[6] J. Latuch, G. Cieslak, H. Dimitrov, M. Krasnowski, T. Kulik, J. Phys.: Conf. Ser. 144 (2009) 1–8.
[7] Ch. Tang, Y. Du, J. Wang, H. Zhou, L. Zhang, F. Zheng, J. Lee, Q. Yao, Intermetallics 18 (2010) 900–906.
[8] D. Vojtěch, K. Saksl, J. Verner, B. Bártová, Mater. Sci. Eng. A428 (2006) 188–195.
[9] D. Vojtěch, A. Michalcová, J. Pilch, P. Šittner, J. Šerák, P. Novák, J. Alloys Compd. 475 (2009) 151–156.
[10] H. Yang, J.Q. Wang, Y. Li, J. Non-Cryst. Solids 354 (2008) 3473–3479.
[11] K. Song, X. Bian, X. Lu, J. Guo, G. Li, M. Xie, Mater. Sci. Eng. A506 (2009) 87–93.
[12] A. Inoue, H. Kimura, J. Light Met. 1 (2001) 31–41.
[13] W.F. Gale, T.C. Totemeier, Smithells Metals Reference Book, 8th edition, Elsevier, 2004.
[14] S.J. Hong, T.S. Kim, C. Suryanayana, B.S. Chun, Met. Mater. Trans. 32A (2001) 821–829.
[15] Ch. Tang, Y. Du, H. Zhou, J. Alloys Compd. 470 (2009) 222–227.
[16] Ch. Tang, Y. Du, H.H. Xu, W. Xiong, L.J. Zhang, F. Zheng, H.Y. Zhou, Intermetallics 16 (2008) 432–439.
[17] B. Bártová, D. Vojtěch, J. Verner, A. Gemperle, V. Studnička, J. Alloys Compd. 387 (2005) 193–200.
[18] Z.H. Huang, J.F. Li, Q.L. Rao, Y.H. Zhou, Mater. Sci. Eng. A489 (2008) 380–388.
[19] M.J. Aziz, T. Kaplan, Acta Metall. 36 (1988) 2335–2347.
[20] A. Brahmi, T. Gerique, M. Torralba, M. Lieblich, Scripta Mater. 37 (1997) 1623–1629.
[21] J.C. Ehrstrom, A. Pineau, Mater. Sci. Eng. A 186 (1994) 55–64.
[22] Y. Wang, Z. Zhang, W. Wang, X. Bian, Mater. Sci. Eng. A 366 (2004) 17–24.